SUPPLEMENTARY INFORMATION

1. LONG PROFILES OF MIOCENE-PLIOCENE CHANNELS

Present-day slope of the base Ogallala Group (OG) and Remsburg Ranch Beds (RRB) were constructed using regional structure contour maps and geological mapping (Swinehart et al., 1985; Swinehart and Diffendal, 1997). Profiles are fit by a least squares regression using an exponential fit to scattered outcrop and well data. The Ogallala-age channels are constructed from superposition of channel positions upon the base-Ogallala structure contour map (Fig. DR1). Error on RRB profile (Fig. 3A) is minimal. The values of fitted parameters and statistical measures for the channels are shown in a Table DR1. North Platte River profile downloaded from http://seamless.usgs.gov/.

2. GRAIN SIZE DATA COLLECTION

Grain size data (D_{50}) were collected by measuring the axes of 100 randomly-selected clasts (>2 mm) in a 1 m^2 area. In situ Wolman point counts at each site were supplemented with a photographic version of the Wolman point count method to increase data collection efficiency. Time-averaged grain size measurements were determined by sampling two to three 1 m^2 grids within a 10 m^2 area (Duller et al., 2010; Whittaker et al., 2011) (Table DR2). AHF and OG data were compared to McMillan et al. (2002) (Fig. DR2). The error on individual point counts is negligible, but the error bars in Fig 2 represent the standard error associated with multiple median grain size values at-a-site.

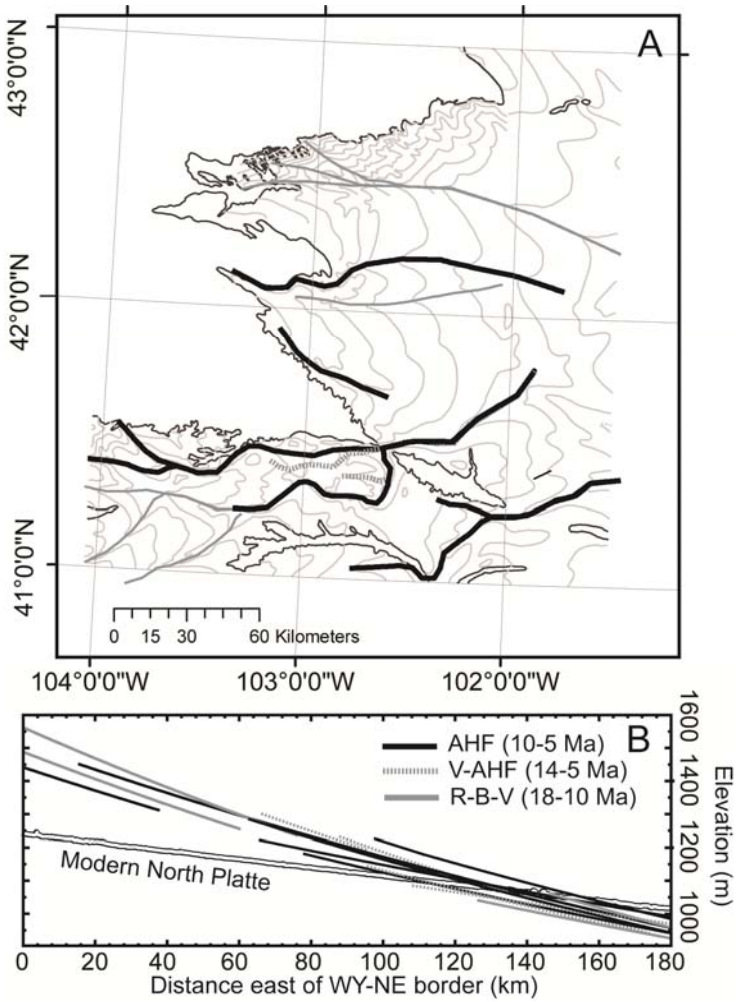

Fig. DR1: Map showing the position of base-Ogallala channels of different age in western Nebraska (A). The long profile of each of these channels in shown in (B) (R; Runningwater Formation, B; Box Butte Formation, V; Valentine Formation, AHF; Ash Hollow Formation).

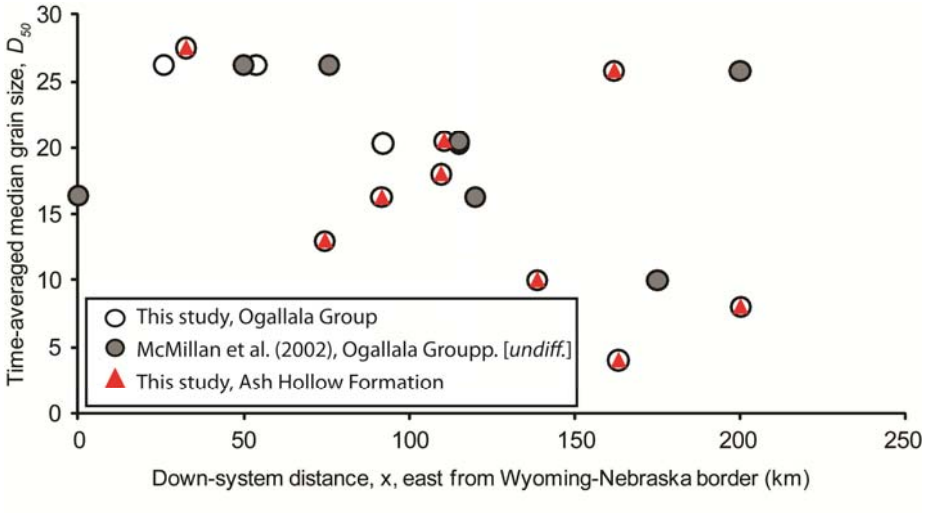

Fig. DR2: D_{50} against downsystem distance in the OG from the data used in the analysis of McMillan et al. (2002) (grey circles) and for this study (open circles). Red triangles show data points in the upper Miocene AHF. Grain size distributions for the AHF (10-6 Ma) are very similar to the data of McMillan et al. (2002) for the undifferentiated OG as a whole (20-6 Ma).

3. PALEODEPTHS

Paleodepth, H, for channels in the OG increase from ~1 to 2 m downsystem over the study area, as implied by McMillan et al. (2002). Heller et al. (2003) measure paleoflow depths from the AHF, and the undifferentiated Ogallala (Table DR3) to be 1.4m ± 0.5(1σ). H estimates by previous workers (e.g. Skinner et al., 1977; Seni, 1980; Diffendal, 1982) and our own field observations agree with these measurements. However AHF channel depth does vary between sites. Conservative end-member solutions of H = 1 m and H = 2 m are used to constrain AHF paleoslope. H in the RRB is reliably constrained in the field from a site 100 km east of the Wyoming-Nebraska border where sedimentary structures suggest a time-averaged flow depth of 1.9 m ±0.4 (1σ). Paleodepths near the Wyoming-Nebraska border are >1.5 m. The downsystem evolution of depth is described as:

$$H = k_1 x^b + H_0 \qquad \text{(S.1.)},$$

where k_1 is a coefficient, and the exponent, b, is 0.4 for rivers displaying typical hydraulic scaling (Leopold et al., 1964). k_1 is calibrated as ~0.02 from field constraints on measured channel depths at a position 100 km east of the Wyoming Nebraska border (Table DR3). H_0 represents the initial flow depth near the WY-NE border, which is ~1.75 m $\pm$ 0.4(1σ). End-member solutions of H = 1.5 m and H = 2 m are used to constrain RRB paleoslope.

4. PALEOSLOPE

Paleoslope is calculated from D_{50} and H measurements, following the Shields Stress inversion approach of Paola and Mohrig (1996) for gravel deposition under fully turbulent flow. The critical dimensionless shear stress to entrain sediment, τ^*_c, (the Shields Stress) normalizes local bed shear stress by a function of the sediment density, ρ_s and the time-averaged median grain size, $\langle D_{50} \rangle$, given by:

$$\tau_c^* = \frac{\langle H \rangle S}{\rho_x \langle D_{50} \rangle} \qquad \text{(S.2.)},$$

where S is the channel slope, ρ_x is the excess sediment density (ρ_s) over water (ρ), expressed as $(\rho_s - \rho)/\rho$. τ^*_c is a constant, typically 0.045-0.06 (Paola and Mohrig, 1996, Mueller and Pitlick, 2005). S and D_{50} are typically configured such that the local shear stress is 1.2 - 1.4 times the critical shear stress to entrain sediment on the bed (Mueller and Pitlick, 2005). Paleoslope $S_{(x)}$ is therefore calculated as:

$$S_{(x)} = \frac{C\rho_x < D_{50} >}{< H >} \qquad \text{(S.3.)},$$

where C = 0.07 (using τ^*_c = 0.05), consistent with previous workers (e.g. Paola and Mohrig, 1996; Mueller and Pitlick, 1995) and $\rho_x \sim 1.6$.

5. UNPAIRED, TWO-TAILED T-TEST OF SLOPES

Unpaired, two-tailed t-tests were used to investigate the likelihood that present-day slopes differ significantly from reconstructed paleoslopes. Specifically, we assess if: (1) the modern and reconstructed paleoslopes of the AHF are different by comparing 31 reconstructed paleoslope values (since H, n = 31) to a present-day individual lower limit (-1σ) AHF slope value (n = 8); (2) the modern and reconstructed paleoslope of the RRB are different by comparing 5 reconstructed paleoslope values (since H, n = 5), to the single present-day RRB slope value; (3) the present-day AHF channels (n = 8) and the present-day older undifferentiated OG channels' (n = 8) paleoslopes are. The results are: (1) the present-day base-AHF and the upper limit of the error associated with the reconstructed base-AHF paleoslopes are significantly different at the 99.95% confidence level (30 d.o.f); (2) The differences between the modern base of the RRB slope and paleoslope reconstructions are most likely (58% with 5 d.o.f) to have occurred purely by chance from the inherent variability in the data, which supports the hypothesis that they are the same; (3) The differences between the measured AHF and older OG paleochannel slopes are most likely (58% with 7 d.o.f) to have occurred purely by chance from the inherent variability in the data, which supports the hypothesis that they are the same.

6. PALEOHYDRAULIC ANALYSES

Downsystem discharge data are estimated using measurements of hydraulic radius, R, (e.g. in the RRB) and by channel slope and depth measurements assuming $R \sim H$. Average flow velocity, U, is approximated by the Manning's Equation:

$$U = \frac{1}{n} R^{2/3} S^{1/2} \qquad \text{(S.4.)},$$

where n is the Manning's roughness coefficient (~0.03). Bank full discharge, Q, is given by:

$$Q = URW \qquad \text{(S.5.)}.$$

Discharge per unit width, $q_w = Q/W$, is expressed as:

$$q_w = \frac{1}{n} R^{5/3} S^{1/2} \qquad \text{(S.6.)}.$$

Complementary estimates of discharge are derived from D_{50} and slope data. Assuming $R \sim H$, rearranging Eq. (S.6.) to solve for depth, and substituting this into Eq. (S.2.) gives:

$$q_w = \left(\frac{\tau^*_c \rho_x < D_{50} >}{n^{3/5} S^{7/10}} \right)^{5/3} \qquad \text{(S.7.)}.$$

Specific stream power (ω) per unit area of the bed is given by:

$$\omega = \rho g q_w S \qquad \text{(S.8.)}.$$

7. ERRORS

The largest uncertainty in our calculations is paleodepth, *H*. *H* for AHF channels lies in the range 1-2 m. For the RRB, downsystem *H* is constrained by a numerical fit to calibrated value (see section 3). These uncertainties are used to define the error bars on data in Fig. 3A and Fig. 3B, and the top part of Fig. 4B. Uncertainty in the q_w calculation in the top panel of Fig. 4B (Eq. S.6) primarily depends on *H* but also the value of Manning's *n*. We use $n = 0.03$ for consistency. The dependence of *n* on grain size (Parker, 1991) for RRB is $n = 0.03 \pm 0.002(1\sigma)$ and for AHF is $n = 0.025 \pm 0.002(1\sigma)$. Our constant *n* assumption (0.03) underestimates q_w by 17% for the AHF, which is small relative to our uncertainty in *H*. For figure 4B (upper panel) a conservative error of ±50% on q_w is implemented for the RRB and AHF, accounting for the 1σ error on paleoflow depth. Uncertainty in the bottom panel of Fig. 4B, where q_w estimates are derived from *S* and grain size (Eq. S.7) include *H* (from which *S* comes), D_{50} (well-characterized) and *n*. We propagate these errors through to produce the bars in the bottom panel of Fig. 4B. We give ±100% error on calculated q_w values for the AHF, and ±40% for the RRB. Uncertainty on stream powers (Eq. S.8) comes from uncertainties in *H* (and hence *S*) and D_{50} (Fig 4C). A 50% to 100% error is used for the RRB, dependant on the variability of D_{50} at a site. The stream power calculation for the AHF necessarily uses reconstructed paleoslope values twice, so data is displayed with generous error bars of ±200%.

8. REFERENCES [not cited in the main article]

Leopold, L., Wolman, G., and Miller, J., 1964, Fluvial processes in geomorphology. W.H. Freeman and Company, San Francisco.

Mueller, E.R., Pitlick, J., and Nelson, J.M., 2005, Variation in the reference Shields Stress for bed load transport in gravel bed rivers and streams: Water Resources, Research, v.41, W04006.

Parker, G., 1991, Selective sorting and abrasion of river gravel II: Applications: Journal of Hydraulic Engineering, v. 117, p. 150-171.

Seni, S.J., 1980, Sand-body geometry and depositional systems, Ogallala Formation, Texas: University of Texas Bureau of Economic Geology Report of Investigations, v. 105, 36 p

Skinner, M.F., Skinner, S.M., and Gooris, R.J., 1977, Stratigraphy and biostratigraphy of late Cenozoic deposits in central Sioux County, western Nebraska: American Museum of Natural History Bulletin, v. 158, 371 p. Portentous.

Stanley, K.O. and Wayne, W.J., 1972, Epeirogenic and climatic controls of early sediment dispersal in Nebraska: Geological Society of America Bulletin, v. 83, p. 3675-3690.

SUPPLEMENTARY DATA TABLES

TABLE DR1: EXPONENTIAL FITS TO BASE-UNIT PROFILES

Profile[1]	Fitted equation[2]	*a*	*b*	R^2	Profile start (km east of WY-NE border)	Profile end (km east of WY-NE border)
RR	$y = ae^{-bx}$	1411	0.00000152	0.99	0	180
AH	$y = ae^{-bx}$	1515	0.00000264	0.98	62	208
AH	$y = ae^{-bx}$	1544	0.00000217	0.91	82	137
AH	$y = ae^{-bx}$	1518	0.00000257	0.97	112	211
AH	$y = ae^{-bx}$	1378	0.00000183	0.96	65	230
AH	$y = ae^{-bx}$	1653	0.00000303	0.92	146	227
AH	$y = ae^{-bx}$	1580	0.00000263	0.98	110	240
AH	$y = ae^{-bx}$	1441	0.00000250	0.76	0	37
R,V,B	$y = ae^{-bx}$	1506	0.00000271	0.98	65	227
R,V,B	$y = ae^{-bx}$	1470	0.00000256	0.96	100	228
R,V,B	$y = ae^{-bx}$	1432	0.00000237	0.96	115	232
R,V,B	$y = ae^{-bx}$	1488	0.00000283	0.95	0	60
R,V,B	$y = ae^{-bx}$	1562	0.00000308	0.97	0	76
R,V,B	$y = ae^{-bx}$	1606	0.00000337	0.92	17	75
R,V,B	$y = ae^{-bx}$	1614	0.00000316	0.97	87	174

[1]RR; Remsburg Ranch beds, AH; Ash Hollow Formation, R; Runningwater Formation, B; Box Butte Formation, V; Valentine Formation, AHF; Ash Hollow Formation

[2] Least squares regression to this an exponential fit was used to derive likely initial elevations at x = 0 (i.e. Wyoming-Nebraska border)

TABLE DR3: PALEO-FLOW DEPTHS FOR STUDY CHANNELS

Unit	H (m)	East of WY-NE border (km)	Unit	H (m)	East of WY-NE border (km)
RR[1]	1.5	10	OG	0.7	84
RR	1.6	10	OG	1.2	84
RR	2	100	OG	1	84
RR	1.8	100	OG	0.65	84
RR	2.2	100	OG	0.65	84
RR	1.5	100	OG	0.8	84
RR	2.5	100	OG	0.8	84
RR	1.5	100	OG	1.2	84
			OG	1	84
OG[2]	1.4	0	OG	1.2	84
OG	1.4	0	OG	0.8	84
OG	1.3	0	OG	0.8	84
OG	1.3	0	OG	1.6	105
OG	1.7	37	OG	1.6	105
OG	1.7	37	OG	1.5	105
OG	1.4	37	OG	1.5	105
OG	1.4	37	OG	1.2	142
OG	2.3	37	OG	1.2	142
OG	2.3	37	OG	0.8	142
OG	1.9	37	OG	2.7	170
OG	1.9	37	OG	2.05	170
OG	1.2	37	OG	1.8	170
OG	1.2	37	OG	3.2	170

[1]RR; Remsburg Ranch beds

[2]OG; Ogallala Group. Including data from Heller et al. (2003)

TABLE DR2: GRAIN SIZE IN REMSBURG RANCH BEDS AND ASH HOLLOW FORMATION

Unit[1]	X[2]	Y[2]	D_{50} (mm)	D_{84} (mm)	Method[3]	Distance E of WY-NE border (km)
RR	-104.203	42.10283	16	27	Wolman	-12724
RR	-103.97	42.03033	23	49	Wolman	7212
RR	-103.718	42.01333	60	112	Wolman	28576
RR	-102.145	41.445	28	52	Wolman	160439
RR	-102.144	41.44583	33	55	Wolman	160800
RR	-102.676	41.56833	33.5	52	Wolman	115194
RR	-103.674	42.00361	52	89	Wolman	31589
RR	-102.488	41.47528	50	80	Wolman	130800
RR	-102.484	41.47667	34	64	Wolman	131582
RR	-102.106	41.25611	50	75	Wolman	163062
RR	-102.677	41.5475	55	98	Wolman	116036
RR	-104.709	42.19083	55	88	Wolman	-51426
RR	-103.97	42.03033	30	48	Photo	7212
RR	-103.718	42.01333	47	71	Photo	28576
RR	-102.144	41.44583	18	2	Photo	160800
RR	-102.488	41.47528	21	32	Photo	130800
RR	-102.677	41.5475	26	46	Photo	116036
RR	-104.709	42.19083	19	28	Photo	-51426
RR	-103.04	41.69406	37	76	Wolman	84709
RR	-103.605	41.97006	33	59	Wolman	37264
RR	-103.605	41.97047	31	48	Wolman	37250
RR	-103.605	41.97103	40	60	Wolman	37080
RR	-104.09	42.17678	69	111	Wolman	-3165
RR	-102.744	41.5725	47	86	Wolman	110350
RR	-102.744	41.57278	41	66	Wolman	110433
RR	-102.734	41.57194	45	81	Wolman	110082
RR	-102.736	41.57333	62	98	Wolman	110390
RR	-103.04	41.69222	41	71	Wolman	85000
RR	-103.041	41.69583	60	92	Wolman	84872
RR	-103.606	41.97222	50	80	Wolman	37261
RR	-103.58	41.96389	36	57	Wolman	39127
RR	-103.589	41.96528	52	91	Wolman	38708
RR	-103.518	41.92528	52	94	Wolman	44509
RR	-103.877	42.08139	36	61	Wolman	14676
RR	-103.876	42.0825	65	113	Wolman	14730
RR	-103.877	42.07306	48	84	Wolman	14676
RR	-103.299	41.82944	40	72	Wolman	63135
RR	-103.299	41.82944	42	63	Wolman	63150
RR	-103.939	42.13139	37	60	Wolman	9423
RR	-103.939	42.13083	41	64	Wolman	9361
RR	-103.951	42.13778	45	75	Wolman	8520
RR	-103.949	42.13444	47	81	Wolman	8690
RR	-104.867	42.18889	48	86	Wolman	-67289
RR	-104.852	42.1875	44	64	Wolman	-66186
RR	-104.849	42.18528	85	143	Wolman	-65900
RR	-104.089	42.17667	45	74	Wolman	-3038
RR	-104.099	42.17778	65	109	Wolman	-3805
RR	-104.107	42.18167	53	85	Wolman	-4400
RR	-104.105	42.18139	58	95	Wolman	-4300
RR	-103.605	41.97103	34	57	Photo	37080
RR	-104.09	42.17678	59	81	Photo	-3165
RR	-102.744	41.5725	29	48	Photo	110350
RR	-102.734	41.57194	33	48	Photo	110082
RR	-102.736	41.57333	30	46	Photo	110390
RR	-103.04	41.69222	27	41	Photo	85000
RR	-103.041	41.69583	31	45	Photo	84872
RR	-103.606	41.97222	28	48	Photo	37261
RR	-103.58	41.96389	25	37	Photo	39127
RR	-103.589	41.96528	26	53	Photo	38708
RR	-103.877	42.08139	23	36	Photo	14676
RR	-103.877	42.07306	15	24	Photo	14676
RR	-103.299	41.82944	20	29	Photo	63135
RR	-103.939	42.13139	24	34	Photo	9423
RR	-103.951	42.13778	21	34	Photo	8520
RR	-103.949	42.13444	22	34	Photo	8690
RR	-104.867	42.18889	39	67	Photo	-67289
RR	-104.864	42.19056	34	59	Photo	-67100
RR	-104.099	42.17778	31	46	Photo	-3805
AH	-103.679	42.12861	27	42	Wolman	32500
AH	-102.742	41.56083	18	23	Wolman	109624
AH	-102.129	41.29352	25	41	Wolman	162000
AH	-102.393	41.36407	10	15	Wolman	138700
AH	-102.957	41.45648	16	28	Wolman	91700
AH	-103.744	41.51875	26	45	Wolman	25845
AH	-103.413	41.49359	26	41	Wolman	53800
AH	-102.741	41.58466	20	34	Wolman	110531
AH	-101.668	41.20425	8	12	Photo	200149
AH	-102.114	41.29156	4	7	Photo	163277
AH	-103.154	41.50531	7	12	Photo	75400
AH	-103.168	41.50656	13	20	Photo	74500

[1]RR; Remsburg Ranch beds, AH; Ash Hollow Formation

[2] XY co-ordinates in longitude/latitude space

[3]Wolman data are field counts of > 100 clasts, repeated several times at each field site. Photo data are measurements of sediment caliber derived from clast point counts on scaled grain size photos of field exposures, repeated several times at each field site.